ELSEVIER

Superlattices and Microstructures 36 (2004) 293–304

Superlattices and Microstructures

www.elsevier.com/locate/superlattices

Efficient phase-field simulation of quantum dot formation in a strained heteroepitaxial film

S.M. Wise[a,*], J.S. Lowengrub[a], J.S. Kim[a], W.C. Johnson[b]

[a] *Mathematics Department, University of California, Irvine, CA, USA*
[b] *Department of Materials Science and Engineering, University of Virginia, Charlottesville, VA, USA*

Available online 23 September 2004

Abstract

A Cahn–Hilliard evolution equation possessing a source term is employed to study the morphological evolution of a strained heteroepitaxial thin film, during continuous mass deposition, on a substrate with an embedded coherent island. The elastic properties and the surface energy are anisotropic, with the surface energy anisotropy being strong enough to result in missing orientations and facets. A sophisticated finite-difference/multigrid method and an implicit time integration scheme are combined to make an efficient numerical method, one which enables numerically tractable computation in both two and three dimensions. Herein we present preliminary two-dimensional results demonstrating the utility of our finite difference/multigrid algorithms. The strain localization effects produced by a buried, coherent inclusion are shown to produce laterally organized quantum dots during the morphological evolution of the film.

Keywords: Thin film; Self-assembly; Substrate; Stress; Anisotropy; Surface diffusion; Epitaxial strain

1. Introduction

The relaxation of strain during heteroepitaxial growth by modification of surface morphology provides a mechanism for influencing the self-organization of quantum dot structures [1,2]. For example, the growth of SiGe on Si at elevated temperatures can lead

* Corresponding author. Tel.: +1949-824-6439; fax: +1949-824-7993.
E-mail address: swise@math.uci.edu (S.M. Wise).

0749-6036/$ - see front matter © 2004 Elsevier Ltd. All rights reserved.
doi:10.1016/j.spmi.2004.08.029

to the formation of stressed islands [3]. The islands form with {510} facets [4] before transitioning to a dome morphology with {310} facets at larger sizes [5]. At lower growth temperatures and depending on the layer composition, different surface morphologies can be observed including the formation of pits and quantum fortress structures [6]. Strain energy stored in the initially planar epilayer can be partially relieved by perturbing the surface morphology [7]. Although this process leads to an increase in the surface energy, the net decrease in free (strain plus surface) energy of the layer is sufficient for the development of islands, pits, or quantum fortress structures.

Strain has also been recognized as a possible mechanism to control both the lateral and vertical self-organization of quantum dot superlattices [8,9]. The strain on the surface induced by an embedded, coherent island affects the diffusion of atoms and the nucleation of new islands on the surface. An embedded island with a positive misfit strain induces a positive, tensile strain on the surface above the island. The elastic strain energy density of the growing epilayer is reduced in this region as compared to unstressed or to compressively stressed regions of the surface. Simple models predict that the lateral spacing between islands becomes more regular as the number of island layers increases [10].

Diffusion on the surface of a stressed thin film is strongly affected by the shape of the surface. Material located in a crest on the surface will possess a more relaxed strain state as compared to material located in a more constrained region such as a valley. These strain gradients induce corresponding gradients in the chemical potential on the surface leading to enhanced mass flow to the surface crests. This process tends to destabilize the surface morphology leading to the growth of islands [7,11].

Recently, Liu, Zhang and Lu [12–15] have performed a series of interesting simulations exploring surface morphological evolution during Stranski–Krastanov heteroepitaxial growth assuming isotropic surface energies. They use a finite element/interface tracking method to solve a surface diffusion problem without allowing for compositional demixing. They show that, depending on various materials parameters, the surface evolves into ripples which then break up into islands, before undergoing a coarsening process. The strain field which arises from the island can permit some self-organization of the particles along the elastically soft crystallographic directions. They also predict that the self-assembly of quantum dots is strongly influenced by the magnitude of the deposition rate [16]. Strain localization effects have been simulated in [13], where the authors considered self-organization of quantum superlattices, assuming isotropic surface energy of the film.

In this paper we present some preliminary, two-dimensional results from a phase field model of quantum dot formation in a strained heteroepitaxial film during continuous mass deposition. We investigate the effect of a strain center produced by an embedded misfitting particle in the substrate. We use the phase field approach of Eggleston et al. [17–19]. We assume that both the film–vapor surface energy and the elasticity of the film and substrate are anisotropic. In fact, the surface energy anisotropy is strong enough to result in missing orientations and facets.

We develop the phase-field equations in nondimensional form and connect the sharp interface and phase-field model parameters. Our work represents an extension of [17–19] in two important ways: first we use an efficient, fully implicit method for integrating in time the Cahn–Hilliard/elasticity system of equations [20–22]. This approach eliminates

the high-order time step restriction for the explicit method used in [17–19], which is a necessary first step towards feasibly performing physically-relevant simulations in three dimensions. In addition, we use conservative, stable spatial discretizations that, unlike the approach in [17], extend straightforwardly to three dimensions. Second, this model allows us to consider both substrate patterning (e.g. mesas and vias) and strain patterning (e.g. embedded particles).

2. Thermodynamics

Herein we use the diffuse interface approach developed in [17–19] for modeling the morphological evolution of a strained epitaxial film on a compliant substrate. In this approach, a conserved order parameter c ($c = 1$ in the film and substrate and $c = 0$ in the vapor) satisfying a generalized Cahn–Hilliard equation is used to describe the interface between the film and vapor phases. A generalized chemical potential μ is used that includes the effects of diffusion and elastic stresses due to the lattice mismatch between the film and substrate. A stationary order parameter ϕ characterizes the topography of the film–substrate interface, where $\phi = 1$ in the substrate, and $\phi = 0$ in both the film and vapor states. A degenerate mobility function is used to constrain diffusion to occur only near the film–vapor interface and deposition is modeled through the inclusion of a source term in the Cahn–Hilliard equation. In two dimensions, the model is given by

$$c_{,t} = \nabla \cdot (M(c,\phi)\nabla\mu) + S(c,\theta), \tag{1}$$

$$\mu = f_{,c}(c) + W_{,c}(c,\phi,E) - \nabla \cdot (\epsilon^2(\theta,\phi)\nabla c + \epsilon(\theta,\phi)\epsilon_{,\theta}(\theta,\phi)\nabla^{\perp}c), \tag{2}$$

where $S(c,\theta)$ is the deposition function, θ is the normal angle of the interface (measured counterclockwise off the x axis), $M(c,\phi)$ is the mobility, $f(c)$ is the Helmholtz free energy density, $W(c,\phi,E)$ is the elastic energy density, E is the linearly elastic strain tensor, $\epsilon(\theta,\phi)$ is the anisotropic surface energy and $\nabla^{\perp}c = (-c_{,y}, c_{,x})^{\mathrm{T}}$ is a vector in the tangential direction to the interface. The unit normal vector $\mathbf{n} = -\nabla c/|\nabla c|$ to the level curves of c is related to the normal angle θ by $\cos(\theta) = n_x$ and $\sin(\theta) = n_y$. Anisotropic interface energy is modeled using the four-fold symmetric function

$$\epsilon(\theta,\phi) = \epsilon_o(1 + \epsilon_4(1-\phi)^4\cos(4\theta)), \tag{3}$$

where ϵ_o is a constant, and ϵ_4 is the anisotropy parameter. Note that for this form, the substrate ($\phi = 1$) has isotropic interfacial energy, which results in the wetting of the substrate by the film.

We take $f(c) = \omega c^2(1-c)^2/4$, which has minima at $c = 0, 1$, and take the $c = 1$ state as the solid phase (both film and substrate) and the $c = 0$ state, the vapor phase. The interface between the film and vapor is identified as the locus of points $\mathbf{x}$ satisfying $c(\mathbf{x}) = 0.5$. The positive constant ω sets the barrier height, and the relationship between ω and ϵ_o is the primary determinant of the interfacial thickness and interfacial energy. In an infinite, one-dimensional, stress-free, isotropic system, Eqs. (1) and (2) admit the steady state solution $c(x) = [1 - \tanh(x/(2\delta))]/2$ [23], with the interfacial "thickness" $\delta = \epsilon_o\sqrt{2/\omega}$, and interfacial energy $\gamma = \epsilon_o\sqrt{\omega/72}$.

We assume that diffusion in the thin film system occurs mainly around the film–vapor interface ($c = 0.5$) and is strictly zero in the substrate and in the "bulk" film regions. An appropriate functional form for the mobility is

$$M(c, \phi) = 6M_s c^2(1 - c)^2(1 - \phi), \tag{4}$$

where M_s is the surface mobility which, as we will see later, can be connected to the film–vapor surface diffusivity D_s.

The deposition function S models the flux of mass from the vapor phase to the film interface. Due to gravity, deposition is assumed to occur in the y-direction so that we take

$$S(c, \theta) = V_d A\mathcal{R}c^2(1 - c)^2 n_y, \tag{5}$$

where V_d is the (spatially constant) surface velocity due to deposition, A is a scale factor chosen below to match the sharp interface result, $\mathcal{R}$ is a random number ($0.9 \leq \mathcal{R} \leq 1.1$) and $c^2(1 - c)^2$ localizes the flux at the film–vapor interface.

Elastic stresses arise in the system due to the lattice mismatch between the film and substrate. Localization of stresses is affected by a number of factors, including the topography of the substrate, buried inclusions, defects in the substrate, and by loss of coherence at the film–substrate interface. In this effort we model the first two factors. Consequently, the elastic energy has the form

$$W(c, \phi, E) = \frac{1}{2} \sum_{i,j=1}^{2} T_{ij}(E_{ij} - \delta_{ij} e(c, \phi)), \tag{6}$$

where the $E_{ij} = (u_{i,j} + u_{j,i})/2$ are the components of the linear strain tensor, $e(c, \phi)$ is the misfit strain, and the T_{ij} are the components of the stress tensor. The strain and stress are related via Hooke's law

$$T_{ij} = \sum_{k,l=1}^{2} \mathcal{C}_{ijkl}(c)(E_{kl} - \delta_{kl} e(c, \phi)), \tag{7}$$

where $\mathcal{C}$ is the cubic elastic stiffness tensor and is assumed to depend only upon the order parameter c. Thus, for simplicity, the film and substrate are taken to have equal elastic stiffness coefficients [18,19]. Also following [18,19] we model the vapor as an elastic solid with very weak elastic stiffness, i.e., $\mathcal{C}_{ijkl}(c = 0) \ll \mathcal{C}_{ijkl}(c = 1)$. Specifically, we use the model [24]

$$\mathcal{C}_{ijkl}(c) = \mathcal{C}^0_{ijkl} + q(c)(\mathcal{C}^1_{ijkl} - \mathcal{C}^0_{ijkl}), \tag{8}$$

where $q(c) = 3c^2 - 2c^3$ is an interpolation function such that $q(1) = 1$, $q(0) = 0 = q'(1) = q'(0)$, and $\mathcal{C}^0_{ijkl}$ and $\mathcal{C}^1_{ijkl}$ are constants satisfying $\mathcal{C}^0_{ijkl} \ll \mathcal{C}^1_{ijkl}$. The misfit strain is modeled as

$$e(c, \phi) = q(c)\eta(1 - \phi), \tag{9}$$

where η is the isotropic misfit strain of the film measured using the substrate as the reference state. Finally, we assume that elastic relaxation occurs on a much faster time

scale than diffusion. Therefore, we use the quasi-static approximation

$$\sum_{j=1}^{2} T_{ij,j} = 0,\ i = 1, 2, \tag{10}$$

where the stresses change in time as a result of the evolving concentration field in the misfit stain.

3. Nondimensionalization and sharp interface scaling

In this section, we present the nondimensional system of equations and discuss the sharp interface limit. This enables us to connect the parameters in the model described above with the true physical constants characterizing the thin-film/vapor system.

Let L be a characteristic length scale of the sample (e.g. $L \approx 200$ nm). Let τ be the characteristic time scale for surface diffusion

$$\tau = L^4/D_s, \tag{11}$$

and let $\eta^2\mathcal{C}_{44}^1$, using the Voigt notation for the cubic elastic constants, be the characteristic scale of the elastic energy density. The evolution is then characterized by the nondimensional quantities

$$\bar{M}_s = \frac{36 M_s \gamma \delta}{D_s},\ \bar{\delta} = \frac{\delta}{L},\ \bar{V}_d = \frac{L^3 V_d}{D_s},\ \epsilon_4, \quad \text{and} \quad Z = \frac{L\eta^2\mathcal{C}_{44}^1}{\gamma}. \tag{12}$$

Denoting the nondimensional variables by an overbar, the nondimensional evolution Eqs. (1) and (2) become

$$c_{,\bar{t}} = \frac{\bar{M}_s}{\bar{\delta}^2}\bar{\nabla}\cdot(\bar{M}(c,\phi)\bar{\nabla}\bar{\mu}) + \frac{\bar{V}_d}{\bar{\delta}}\bar{A}\bar{S}(c,\theta), \tag{13}$$

$$\bar{\mu} = \bar{f}_{,c}(c) + \bar{\delta}\frac{Z}{6}\bar{W}_{,c}(c,\phi,E) - \bar{\delta}^2\bar{\nabla}\cdot(\bar{\epsilon}^2(\theta,\phi)\nabla c + \bar{\epsilon}(\theta,\phi)\bar{\epsilon}_{,\theta}(\theta,\phi)\bar{\nabla}^{\perp}c), \tag{14}$$

where $A = \bar{A}/\delta$ and

$$\bar{M}(c,\phi) = c^2(1-c)^2(1-\phi),\ \bar{S}(c,\theta) = \mathcal{R}c^2(1-c)^2\sin(\theta) \tag{15}$$

$$\bar{f}(c) = \frac{1}{2}c^2(1-c)^2,\ \bar{W}(c,\phi,E) = \frac{1}{2}\sum_{i,j=1}^{2}\bar{T}_{ij}(E_{ij} - \delta_{ij}\bar{e}(c,\phi)), \tag{16}$$

$$\bar{T}_{ij} = \sum_{k,l=1}^{2}\bar{\mathcal{C}}_{ijkl}(c)(E_{kl} - \delta_{kl}\bar{e}(c,\phi)),\ \bar{\mathcal{C}}_{ijkl} = \mathcal{C}_{ijkl}/\mathcal{C}_{44}^1, \tag{17}$$

$$\bar{e}(c,\phi) = q(c)(1-\phi), \quad \text{and} \quad \bar{\epsilon}(\theta,\phi) = 1 + \epsilon_4(1-\phi)^4\cos(4\theta). \tag{18}$$

It remains to determine $\bar{M}_s$ (hence M_s) and $\bar{A}$ to complete the description of the system. To determine these parameters, we consider the sharp interface limit $\bar{\delta} \to 0$. Under the above scaling, the nondimensional sharp interface evolution equations governing the film–vapor interface are

$$V = -\tilde{\epsilon}(\theta(s))\left(\frac{\partial^2 \mu_\Sigma}{\partial s^2} + \bar{V}_d \mathcal{R}\sin(\theta(s))\right), \tag{19}$$

$$\mu_\Sigma = \left(\tilde{\epsilon} + \frac{\partial^2 \tilde{\epsilon}}{\partial \theta^2}\right)\kappa + Z g^{el}, \tag{20}$$

where V is the normal velocity, $\theta(s)$ is the sharp interface normal angle, $\tilde{\epsilon}(\theta) = 1 + \epsilon_4 \cos(4\theta)$ is the anisotropic surface energy, μ_Σ is the chemical potential, κ is the mean curvature of the interface and

$$g^{el} = \frac{1}{2} T^1_{ij}(E^1_{ij} - \delta_{ij}) - \frac{1}{2} T^0_{ij} E^0_{ij} + T^0_{ij}(E^0_{ij} - E^1_{ij}) \tag{21}$$

is the local elastic energy density (e.g. see [25]).

By combining the matched asymptotic expansion procedures outlined in [26,24] and [27] to obtain the sharp interface limit, we find that the leading order normal velocity of the film–vapor interface from Eqs. (13) and (14) is

$$V = -\hat{M}_s \frac{\partial^2 \mu_\Sigma}{\partial s^2} + \bar{V}_d \hat{A} \mathcal{R}\sin(\theta(s)) \tag{22}$$

$$\mu_\Sigma = \Omega\left(\tilde{\epsilon}(\theta(s)) + \frac{\partial^2 \tilde{\epsilon}}{\partial \theta^2}\right)\kappa + \frac{Z}{6} g^{el} \tag{23}$$

where

$$\hat{M}_s = \bar{M}_s \int_{-\infty}^{+\infty} \bar{M}(\hat{c}^{(0)}(z), 0)\, \mathrm{d}z, \tag{24}$$

$$\hat{A} = \bar{A} \int_{-\infty}^{+\infty} (\hat{c}^{(0)}(1 - \hat{c}^{(0)}))^2\, \mathrm{d}z, \tag{25}$$

$$\Omega = \tilde{\epsilon}(\theta(s)) \int_{-\infty}^{+\infty} (\hat{c}^{(0)})^2\, \mathrm{d}z, \tag{26}$$

and $\hat{c}^{(0)}(z)$ is the leading order inner solution where z is the normal coordinate across the interface region. The leading order equation that determines $\hat{c}^{(0)}(z)$ is

$$\bar{f}'(\hat{c}^{(0)}) - \tilde{\epsilon}^2(\theta(s)) \frac{\partial^2 \hat{c}^{(0)}}{\partial z^2} = 0. \tag{27}$$

From this equation, together with far-field matching conditions and the definition of $\bar{f}(c)$, we obtain $\hat{M}_s = \tilde{\epsilon}(\theta)\bar{M}_s/6$, $\hat{A} = \tilde{\epsilon}(\theta)\bar{A}/6$, and $\Omega = 1/6$. Putting everything together, matching the leading order Eqs. (22) and (23) with the corresponding sharp interface Eqs. (19) and (20) requires that $\bar{A} = 6$ and $\bar{M}_s = 36$. This implies that the dimensional mobility $M_s = D_s/(\gamma\delta)$.

The matched asymptotic expansion results presented above assume that the film–vapor interface is smooth (which also implies that the anisotropic surface tension $\tilde{\epsilon} + \partial^2 \tilde{\epsilon}/\partial\theta^2 \geq 0$). The details of the procedure will be presented in a forthcoming paper.

4. Numerical methods

We solve $\sum_{j=1}^{2} \bar{T}_{ij,j} = 0$ and the nondimensional evolution Eqs. (13) and (14) using nonlinear multigrid methods originally developed for Cahn–Hilliard equations by Kim, Kang and Lowengrub [20,21] and their extensions to elastic systems by Wise, Kim and Johnson [22]. These algorithms are based on splitting the fourth order Cahn–Hilliard equation into two second order equations and solving for the concentration and chemical potential simultaneously using second order accurate discretizations in time and space. The spatial discretizations use centered differences and are conservative. The time discretizations are based on generalizations of the Crank–Nicholson algorithm and are fully implicit, thus eliminating the high (fourth) order time step restrictions (i.e., $\Delta t \leq C\Delta x^4$). In certain cases, it is possible to rigorously prove that the resulting numerical schemes converge and that the schemes inherit a discrete version of the continuous energy functional for any time and space step sizes.

To solve the nonlinear discrete system, a nonlinear full approximation storage (FAS) method is used. In the FAS method, as in linear multigrid methods, the errors in the solution are smoothed so that they may be approximated on a coarser grid. An analogue of the linear defect equation is transformed to the coarse grid. The coarse grid corrections are interpolated back to the fine grid where the errors are then smoothed. Because the system is nonlinear, one does not work directly with the errors but rather with full approximations to the discrete solution on the coarse grid. The nonlinearity is treated using one step of Newton's iteration. A pointwise Gauss–Seidel relaxation scheme is used as the smoother in the multigrid method. This corresponds to a local instead of global linearization of the nonlinear scheme and is much more efficient than standard Newton–Gauss–Seidel linearization schemes.

The convergence of our multigrid algorithms is achieved with $\Delta t \leq \Delta t_0$, where Δt_0 depends only on the physical parameters and not on the mesh size. Typically we find that our algorithms are 100 times faster than corresponding explicit methods.

The conservative algorithms described above perform very well, even in the presence of strong interfacial anisotropy. In particular, it can be shown that the conservative spatial discretization enhances stability and that it is possible to construct schemes that have discrete (anisotropic) energy functionals. Interestingly, we find that when the anisotropy is such that the sharp interface surface tension $\tilde{\epsilon} + \partial^2\tilde{\epsilon}/\partial\theta^2 < 0$ for some θ, the conservative discretization remains stable even without convexification of the $1/\tilde{\epsilon}$ plot as was done by Eggleston, McFadden and Voorhees in [17]. This is surprising because linearizing the equations about these values of θ leads to terms involving backwards fourth order diffusion in Eqs. (13) and (14). However, an analysis shows that there are other potentially stabilizing fourth order terms in the equation. Indeed, due to the energy functional, the evolution is highly constrained. For example, it can be shown that the stability of the discrete conservative algorithm even in the presence of such strong anisotropy follows directly from the presence of the discrete energy functional. Using centered differences in the multigrid scheme adds some numerical diffusion to the algorithm, which results in some rounding of the corners, regularizing (smoothing) the numerical solution. In some cases it is desirable to add some further smoothing in the form of a sixth-order diffusion term, although this is not necessary for the simulations presented in the following section.

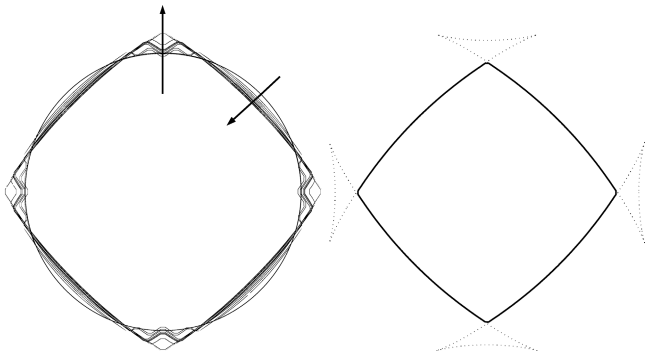

Fig. 1. Evolution from an initially circular particle (left) and the resulting equilibrium shape (right) with the Wulff shape (dotted). The surface anisotropy factor is $\epsilon_4 = 0.2$ and there are no elastic forces ($Z = 0$).

We plan to discuss the numerical issues and the full details of the conservative multigrid algorithm in a forthcoming article.

5. Preliminary simulation results

We begin with a validation of our numerical algorithm for strongly anisotropic systems. In Fig. 1, we present the evolution from an initially circular particle under strong interfacial anisotropy, $\epsilon_4 = 0.2$, and in the absence of elastic forces ($Z = 0$). In particular, $\bar{\delta} = 0.0053$, $N_x = N_y = 128$ and the computational domain is the unit square. In the left-hand figure, the evolution is shown with the evolution direction being indicated by the arrows. The $\langle 11 \rangle$ orientations have the lowest energy. At early stages, the particle develops a wave-pattern with $\langle 11 \rangle$ facets on those surfaces possessing an approximate $\langle 10 \rangle$ orientation. During the later stages of evolution, the waves disappear and a notch develops along $\langle 10 \rangle$. This notch grows outward, eventually leading to the development of the convex, facetted equilibrium particle shape shown on the right. Also plotted on the right-hand side as a dotted line is the corresponding Wulff shape. There is excellent agreement between the calculated Wulff shape and the particle shape obtained by numerical evolution. The calculated evolution shown in Fig. 1 is quite similar to that calculated by Eggleston, McFadden and Voorhees [17], although the exact wave pattern at early times is slightly different, due principally to the fact that we do not convexify the $1/\epsilon$ plot.

Figures 2 and 3 show the morphological evolution of a strained thin film on a substrate during continuous mass deposition. Parameters for the simulations are given in Table 1. The sizes of the computational domains are $6.4L \times 3.2L$, where $L = 50$ nm, and the grid resolution for both simulations is 128×64. The initial conditions for the simulations in Figs. 2 and 3 are the same, but for the addition of a coherent embedded inclusion ($(c, \phi) = (1, 0)$) in Fig. 3. The embedded inclusion and the deposited film have the same misfit strain. Periodic boundary conditions are assumed on the right and left sides of the computational domain. In Fig. 3, these boundary conditions simulate a periodic array of buried inclusions.

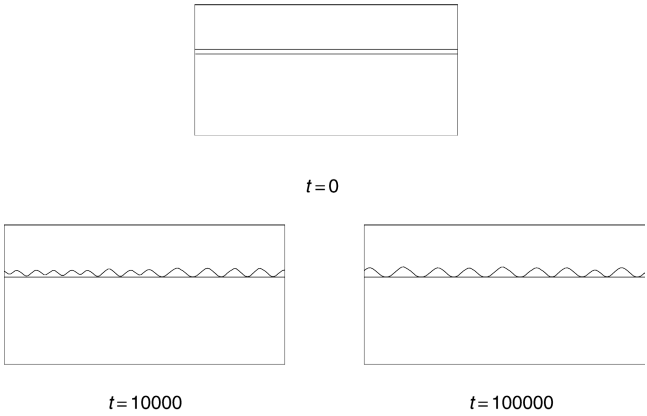

Fig. 2. Evolution of a strained epitaxial thin film to nondimensional time $t = 10^5$. The parameters for the simulation are given in Table 1. Shown are the $c = 0.5$ and $\phi = 0.5$ level sets. From top to bottom the regions represented are the vapor ($(c, \phi) = (0, 0)$), film ($(c, \phi) = (1, 0)$), and substrate ($(c, \phi) = (1, 1)$) phases. Due to the misfit between film and substrate and the surface anisotropy, the film's surface becomes unstable and islands form uniformly along the substrate. Subsequent to island formation, coarsening occurs on a very long time scale.

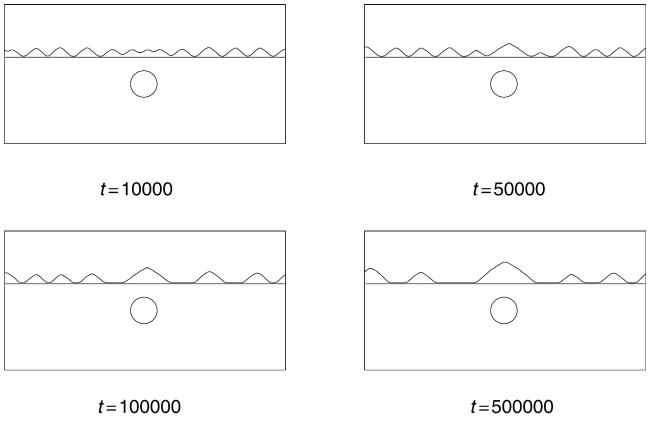

Fig. 3. The evolution of a strained thin film above a buried circular inclusion to nondimensional time $t = 5 \times 10^5$. The simulation parameters are given in Table 1. The dynamics at early times are similar to those in Fig. 2. But, since the inclusion ($(c, \phi) = (1, 0)$) has the same misfit strain as the film, a large, isolated dot grows preferentially above the embedded inclusion, at the expense of nearby neighboring islands.

At very early times, the film evolutions are similar. The anisotropic surface energy initially destabilizes the flat film–vapor interface leading to the formation of islands on the substrate. The islands develop $\langle 11 \rangle$ facets due to the strong anisotropy of the surface energy. Subsequently, in Fig. 2, rapid coarsening occurs until the islands reach an intermediate size determined by the competition between elastic and surface forces. After this stage

Table 1
Parameters for the simulations shown Figs. 2 and 3

Physical		Nondimensional	
$\mathcal{C}_{11}^1$	3.31×10^{11} Pa	$\bar{M}_s$	36
$\mathcal{C}_{12}^1$	1.25×10^{11} Pa	$\bar{A}$	6
$\mathcal{C}_{44}^1$	1.58×10^{11} Pa	$\bar{\delta}$	0.025
γ	1.602 J/m^2	Z	5.8
δ	1.24×10^{-9} m	$\bar{V}_d$	1.26
ϵ_4	0.15		
η	0.0347		
L	50×10^{-9} m		
V_d	$1.008 \times 10^{22} D_s$ m^3		

of evolution, coarsening continues on a very long time scale, and the wavelength of the surface pattern slowly increases in time [18,19].

After the initial formation of islands, the evolution depicted in Fig. 3 is significantly different from that shown in Fig. 2. The buried inclusion expands and stresses the lattice of the substrate above it, due the positive misfit strain (same as film). Thus it requires less elastic energy to nucleate and grow an island above the inclusion, compared to anywhere else on the substrate. Consequently, mass accumulates above the misfitting particle and a large, isolated dot grows preferentially at the expense of its nearest neighbors. Smaller satellite islands far from the isolated dot persist, although their stability at long times under continued deposition needs to be further investigated. Note that the film wets the substrate between the islands, due to the assumed form of the interfacial energy coefficient $\epsilon(\theta, \phi)$.

6. Summary and future work

In this paper we have given some preliminary, two-dimensional results from a phase field model of quantum dot formation in a strained epitaxial film. We developed the equations in nondimensional form and connected the sharp interface and phase-field model parameters. We demonstrated the feasibility of our highly efficient finite difference/multigrid algorithms for solving the phase-field equations numerically. These methods, which rely on conservative spatial discretizations and implicit time integration, are typically 100 times faster than corresponding explicit methods. We showed that our algorithms accurately calculate the proper morphological evolution and equilibrium shapes resulting from high interfacial anisotropy, without the need for regularizing the $1/\epsilon$ plot and without resorting to one-sided differentiation. We then demonstrated the localizing effects of a buried, coherent inclusion on the morphological evolution of the film. The corresponding morphological evolution (Fig. 3) is quite complex. In particular, the evolution of the film depends on a number of parameters specific to the inclusion, including the particle's radius, misfit, depth, etc.

The localizing effects of the embedded particle (strain patterning) are expected to be qualitatively similar to those of the substrate "mesa" (topographical patterning) considered in [18,19]. The localizing effects that arise in both approaches can yield a more ordered

array of islands than in a film without such patterning. There may be cases where modifying the substrate topography is undesirable or impractical. In such cases strain patterning may be the only viable method for effecting organized formation of quantum dots. An in-depth study of strain patterning, in combination with topographic substrate patterning, is underway for both two- and three-dimensional systems.

Acknowledgements

We thank Vittorio Cristini for helpful discussions. We are grateful to the U.S. National Science Foundation for the financial support of this work through the Center for the Design of Nanoscopic Materials, Grant DMR0080016.

References

[1] R. Asaro, W. Tiller, Interface morphology development during stress-corrosion cracking 1: via surface diffusion, Metall. Trans. 3 (1972) 1789.
[2] D. Srolovitz, On the stability of surfaces of stressed solids, Acta Metal. 37 (1989) 621.
[3] D. Eaglesham, M. Cerullo, Dislocation-free Stranski–Krastanov growth of Ge on Si(100), Phys. Rev. Lett. 64 (1990) 1943.
[4] Y.-W. Mo, D. Savage, B. Swartzentruber, M. Lagally, Kinetic pathway in Stranski–Krastanov growth on Ge on Si(001), Phys. Rev. Lett. 65 (1990) 1020.
[5] F. Ross, R. Tromp, M. Reuter, Transition states between pyramids and domes during Ge/Si island growth, Science 286 (1999) 1931.
[6] J. Gray, R. Hull, J. Floro, Control of surface morphology through variation of growth rate in SiGe/Si(100) epitaxial films: nucleation of “quantum fortresses”, Appl. Phys. Lett. 81 (2002) 2445.
[7] M. Grinfeld, Stability of heterogeneous equilibrium in systems containing solid elastic phases, Dokl. Akad. Nauk SSSR 265 (1982) 836.
[8] J. Tersoff, Step energies and roughening of strained layers, Phys. Rev. Lett. 74 (1995) 4962.
[9] C. Teichert, M. Lagally, L. Peticolas, J. Bean, J. Tersoff, Stress-induced self-organization of nanoscale structures in SiGe/Si multilayer films, Phys. Rev. B 53 (1996) 16334.
[10] J. Tersoff, C. Teichert, M. Lagally, Self-organization in growth of quantum dot superlattices, Phys. Rev. Lett. 76 (1996) 1675.
[11] J. Guyer, P. Voorhees, Morphological stability of alloy thin films, Phys. Rev. B 54 (1996) 11710.
[12] Y. Zhang, S. Xu, C.-H. Chiu, Vertical self-alignment of quantum dots in superlattice, Appl. Phys. Lett. 74 (1999) 1809.
[13] P. Liu, Y. Zhang, C. Lu, Self-organized growth of three-dimensional quantum-dot superlattices, Appl. Phys. Lett. 80 (2002) 3910.
[14] P. Liu, Y. Zhang, C. Lu, Formation of self-assembled heteroepitaxial islands in elastically anisotropic films, Phys. Rev. B 67 (2003) 165414.
[15] P. Liu, Y. Zhang, C. Lu, Computer simulation of the Stranski–Krastanov growth of heteroepitaxial films with elastic anisotropy, Surf. Sci. 526 (2003) 375.
[16] Y. Zhang, Self-organization, shape transition, and stability of epitaxially strained islands, Phys. Rev. B 61 (2000) 10388.
[17] J. Eggleston, G. McFadden, P. Voorhees, A phase-field model for highly anisotropic interfacial energy, Physica D 150 (2001) 91–103.
[18] J. Eggleston, Phase field models for thin film growth and Ostwald ripening, Ph.D. Thesis, Northwestern University, Evanston, IL, 2001.
[19] J. Eggleston, P.W. Voorhees, Ordered growth of nanocrystals via a morphological instability, Appl. Phys. Lett. 80 (2) (2002) 306–308.
[20] J. Kim, K. Kang, J. Lowengrub, Conservative methods for Cahn–Hilliard fluids, J. Comput. Phys. 193 (2003) 511.

[21] J. Kim, K. Kang, J. Lowengrub, Conservative multigrid methods for ternary Cahn–Hilliard systems, Commun. Math. Sci. 2 (2004) 53.
[22] S. Wise, J. Kim, W. Johnson, Surface-directed spinodal decomposition in a stressed, two-dimensional thin film, J. Thin Solid Films (in press).
[23] J.W. Cahn, J.E. Hilliard, Free energy of a nonuniform system i: interfacial free energy, J. Chem. Phys. 28 (2) (1958) 258–267.
[24] H.-J. Jou, P. Leo, J. Lowengrub, A diffuse interface model for microstructural evolution in elastically stressed solids, Acta Mater. 46 (1998) 2113.
[25] J. Eshelby, Elastic energy-momentum tensor, J. Elasticity 5 (1975) 321.
[26] J. Cahn, C. Elliott, A. Novick-Cohn, The Cahn–Hilliard equation with a concentration dependent mobility: motion by minus the Laplacian of the mean curvature, Eur. J. Appl. Math. 7 (1996) 287.
[27] G. McFadden, A. Wheeler, R. Braun, S. Coriell, Phase-field models for anisotropic interfaces, Phys. Rev. E 48 (1993) 2016.